

MANEUVER DESIGN AND FLIGHT CONTROL FOR A MARTIAN PROBE NETWORK

Samuel W. Albert* and Hanspeter Schaub†

Motivated by a need for lower-cost planetary science missions to Mars, this study considers the problem of co-delivering a network of small rough landers to the Martian surface. The Small High Impact Energy Landing Device (SHIELD), a vehicle concept under development at NASA JPL, is used as a reference design and a flight mechanics analysis is performed to ensure requirements are met under the influence of relevant uncertainties. Previous results for linearized targeting of regional networks are briefly summarized. A nonlinear targeting method is then developed for large-scale networks for which linearized targeting is inadequate. After exploring relationships between jettison speed, jettison time, and desired landing separation, a Monte Carlo analysis is performed to quantify the robustness of the identified trajectories to relevant uncertainties.

INTRODUCTION

Entry, descent, and landing (EDL) systems for Mars missions are complex, and typically involve multiple mission-critical subsystems that must operate autonomously in harsh conditions.¹ Bringing the risks associated with these subsystems down to acceptable levels is a significant engineering challenge, and this is one reason why, as the size and complexity of payloads to the Martian surface have increased over time, mission costs have also increased.² The top priority for Mars surface missions in this decade is Mars Sample Return (MSR), a multi-mission campaign estimated to cost \$3.8-\$4.4B from formulation through launch and requiring significant technology development.³ It is in this context that a community of planetary scientists and engineers is seeking lower-cost mission concepts and delivery vehicles to enable a sustained program of Mars surface exploration during and after MSR, as outlined in a recent report from the Keck Institute for Space Studies (KISS).⁴

One mission category examined by the KISS study as a potential pathway to reduced cost is networks of small, fixed landers without requirements for surface mobility and with tolerance for relatively high g-loads at landing.⁴ These network missions are of growing interest for a variety of investigations, including atmospheric science and seismology.⁴⁻⁷ In some cases, relevant instruments can be built at small size (5-15 kg) and high g-load tolerance (1,000-2,000 Earth g's).^{8,9} In general, for these mission concepts the probes must be delivered to a surface arrangement with roughly the right size and shape but precision landing is unimportant. Notionally, a probe network

*PhD Candidate, Ann and H.J. Smead Department of Aerospace Engineering Sciences, University of Colorado Boulder, 431 UCB, Colorado Center for Astrodynamics Research, Boulder, CO 80309. AIAA Student Member.

†Professor and Department Chair, Schaden Leadership Chair, Ann and H.J. Smead Department of Aerospace Engineering Sciences, University of Colorado, Boulder, 431 UCB, Colorado Center for Astrodynamics Research, Boulder, CO, 80309. AAS Fellow, AIAA Fellow.

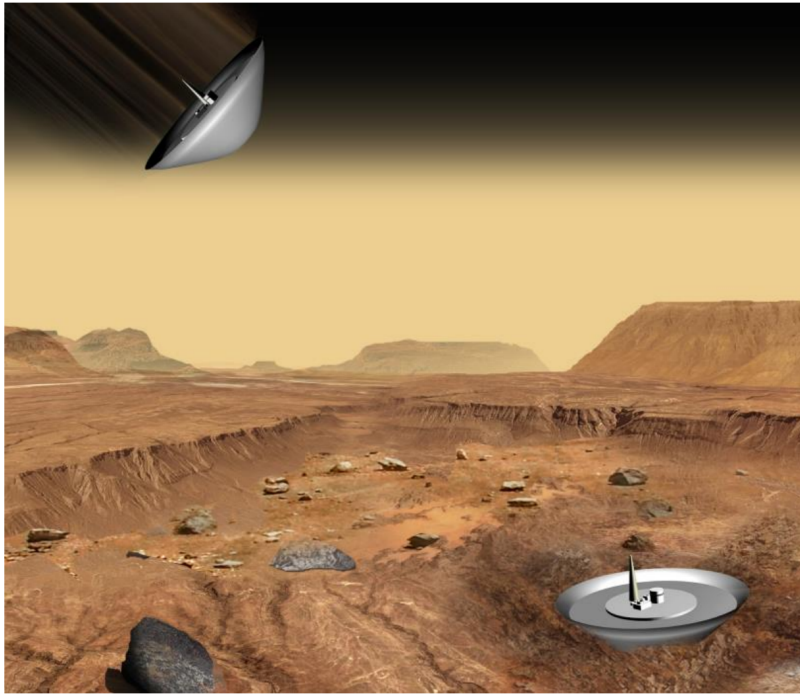


Figure 1: SHIELD concept image¹⁹

would consist of 4-8 probes delivered to Mars by a single carrier spacecraft, and networks of regional (10's of km), mid-range (100's of km), and global sizes are all potentially of interest. A wide variety of network missions for Mars have been proposed,¹⁰⁻¹⁶ but none have come to fruition.

The characteristics of probe network missions enable small, simplified landing platforms with minimal flight-control requirements. The Small High Impact Energy Landing Device (SHIELD) is a vehicle concept under development at the NASA Jet Propulsion Laboratory (JPL) that would meet these needs.¹⁷ The purpose of SHIELD would be to deliver payloads of about 5 kg to the Martian surface at greatly reduced cost and complexity; these reductions would be achieved by eliminating EDL subsystems wherever possible, relying entirely on a passive aeroshell-only entry system followed by a hard landing attenuated by crushable material, notionally resulting in landing decelerations on the order of 1,000 Earth g's.¹⁷ As a point of comparison, the expected landing g-load for the Mars Microprobes was 30,000 g's.¹⁸

Mission complexity may be further reduced if all of the probes could be co-delivered by a single carrier spacecraft onto their uncontrolled entry trajectories, providing necessary resources to the probes during cruise and eliminating the need for attitude control or propulsion subsystems on the probes. The timing, magnitude, and direction of each probe's separation from the carrier spacecraft is an aspect of mission design faced with competing requirements. On the one hand, the later the probe separation the less time there is for the impact of any separation maneuver error to accrue, and the less battery life required for the probe to survive between separation and landing. On the other hand, the earlier the probe separation the smaller the magnitude required for separation velocity and the more time to estimate and correct any error introduced to the carrier spacecraft by separation. Moreover, some networks may be too large in size for co-delivery to be practical, requiring instead multiple maneuvers or multiple carrier spacecraft.

This study begins by presenting a flight-mechanics analysis for the SHIELD probe, considering event timing, landing accuracy, and the effect of varying entry flight-path angles. The problem of co-delivering probes to form a surface network is then considered. First, results from previous work considering regional networks are summarized here, then new results considering large-scale networks are presented and discussed. In both cases, Monte Carlo analyses are performed to capture the impact of relevant uncertainties, including separation maneuver execution error, on the feasibility of the computed co-delivery trajectories.

PROBLEM SETUP

The following assumptions are made for the purpose of this study:

- Each probe is a ballistic rough lander, and is passive other than drag skirt deployment and heatshield jettison.
- Precision landing is not required, but the network should approximate a desired distribution and location on the surface.
- The probes approach Mars on a single carrier spacecraft on an entry trajectory, and the separation events do not change the carrier’s trajectory and no other maneuvers are performed.
- The probes separate from the carrier mechanically.
- Probe jettisons occur between 0.25 and 20 days before atmospheric entry.
- The carrier spacecraft has an approach trajectory such that the magnitude of the planet-relative velocity at the atmospheric entry interface altitude of 125 km is 6 km/s.

Approach trajectories in this study are defined by their entry state, that is the position and velocity of the carrier spacecraft at entry at 125 km altitude. This state is defined by altitude, longitude, latitude, planet-relative velocity V , flight-path angle γ , and heading angle; flight-path angle is the angle between the velocity vector and local horizontal, and heading angle is the angle between the horizontal projection of the velocity vector and a due-North vector in that same plane (e.g. a 90° heading angle is due-East). The central landing site is then the point on the surface where a SHIELD probe would nominally land after continuing on this trajectory. Two things should be noted about this convention. First, because of the separation maneuvers each probe will actually enter the atmosphere with some different state, potentially resulting in significantly different entry flight-path angle (EFPA) and entry velocity values. Second, the carrier spacecraft would not itself be a SHIELD lander and need not actually enter the atmosphere at all; the carrier’s entry state and central landing site are simply convenient ways to define the approach trajectory and a reference point on the surface, respectively.

Separation events are assumed to impart an impulsive change in velocity to the probe, where the jettison velocity \mathbf{V}_j is defined as the velocity of the probe relative to the carrier the moment after separation and jettison speed is defined as the magnitude $V_j = |\mathbf{V}_j|$. This notation is used to distinguish from impulsive $\Delta\mathbf{V}$ because, while they are theoretically equivalent events, this study assumes jettisons occur mechanically (e.g. a spring jettison) rather than propulsively.

Though mostly passive, SHIELD does go through three different entry configurations from atmospheric interface to surface. First, in its *entry* configuration SHIELD is entirely within its protected aeroshell, and this configuration is maintained through the hypersonic and high-heating portion of the flight. Next, SHIELD enters the *descent* configuration soon after beginning subsonic flight by deploying a drag skirt, the purpose of which is to reduce the terminal velocity of the vehicle. Shortly thereafter, the *landing* configuration is initiated with jettison of the heatshield. SHIELD is assumed

to fly at a trim zero angle of attack and has an axisymmetric shape with balanced center of mass, resulting in a lift-to-drag ratio of $L/D = 0$. The drag properties of SHIELD are linearly interpolated based on Mach number from tabular data provided by the JPL SHIELD team, resulting in ballistic coefficients ranging from about 20 kg m^{-2} in the entry configuration down to around 5 kg m^{-2} in the landing configuration. Ballistic coefficient describes the ratio of inertial to aerodynamic forces and is defined as $\beta = m/(C_D A)$ where m is mass, C_D is drag coefficient, and A is aerodynamic reference area. SHIELD is assumed to have a nose radius of $R_n = 0.85 \text{ m}$.

Table 1 summarizes the relevant uncertainties applied throughout this study. Variability of atmospheric density is modeled by using random profiles of density vs. altitude that are generated using the 2010 version of the Mars Global Reference Atmospheric Model (Mars-GRAM 2010).²⁰ Uncertainty in the approach trajectory of the carrier spacecraft is modeled by dispersing the state at atmospheric entry for each trial, then back-propagating the dispersed state to the time of first jettison. The entry flight-path angle γ_0 and entry velocity magnitude V_0 are dispersed independently according to Gaussian distributions centered at the nominal value and with some standard deviation σ . For this study, the 3σ value for γ_0 is set equal to the requirement on delivery error for MSL, and the 3σ value for V_0 is set equal to the required knowledge accuracy at EDL guidance system initialization for MSL.²¹ For a given trial, these three dispersions are applied once, such that all probes experience the same atmosphere and carrier spacecraft trajectory. The ballistic coefficient of each probe is dispersed along a uniform distribution with bounds at $\pm 5\%$ of the nominal value; the lift-to-drag ratio always remains at its nominal value of zero, assuming that axisymmetric spin removes the effect of any small, unintended lift force. Finally, the magnitude of the jettison event is dispersed along a uniform distribution with bounds at $\pm 10\%$ of the nominal value; the direction of the jettison velocities are assumed to be nominal for the purpose of this study. These two dispersions are applied independently to each probe for each trial.

Trajectories are computed via numerical propagation using explicit Runge-Kutta integration of order 4(5) for a rotating ellipsoidal planet. Mars is assumed to have gravitational parameter $\mu = 4.305 \times 10^4 \text{ km}^3 \text{ s}^{-2}$, equatorial radius $R = 3397.2 \text{ km}$, oblateness spherical harmonic coefficient $J_2 = 0.001964$, and a planetary rotation period of $\omega_p = 1.02595675 \text{ days}$.²² The equations of motion for the planet-relative state are provided in the appendix. Mach number is defined as the ratio of vehicle speed to the speed of sound $M = V/a$, where sound speed a for the Martian atmosphere is interpolated from a nominal tabular model.²³ Heat flux is modeled by computing convective heat flux \dot{q} at the stagnation point assuming a fully catalytic surface using the Sutton-Graves expression shown in Eq. 1, where ρ is density and a value of the heating coefficient $k = 1.904 \times 10^{-4} \text{ kg}^{0.5}/\text{m}$ is used based on nominal atmospheric composition at Mars.²⁴

$$\dot{q} = k \sqrt{\frac{\rho}{R_n}} V^3 \quad (1)$$

Table 1: Monte Carlo analysis input dispersions

Parameter	Dispersion
atmospheric density ρ	MarsGRAM
entry velocity magnitude V_0	$3\sigma = 2\text{m/s}$
entry flight-path angle γ_0	$3\sigma = 0.2^\circ$
probe ballistic coefficient β	$\pm 5\%$
jettison speed V_j	$\pm 10\%$

Finally, sensed deceleration (or g-load) is computed as $g = \sqrt{L^2 + D^2}/g_0$ where L and D are the accelerations due to lift and drag, respectively, and g_0 is the standard acceleration due to gravity at the Earth's surface.

SHIELD FLIGHT MECHANICS

Before investigating co-delivery of networks, in this section a flight mechanics analysis is presented for the atmospheric flight of a single SHIELD probe. Analysis is performed at several representative entry flight-path angles: -12° , -18° , and -24° . First, EDL event timing is considered. Drag skirt deployment and heatshield jettison are constrained by three parameters: maximum Mach number at drag skirt deployment, maximum impact velocity, and minimum time between deployment and jettison. The assumed values for these requirements are summarized in Table 2. The combined result of these parameters defines an acceptable range for the timing of each event for any entry trajectory, and the nominal event times can then be selected from within this range. The resulting bounds on event timing were computed for an EFPA of -18° , and were found to be 105.7 seconds after entry (denoted E+105.7 s) for earliest deployment and E+170.9 s for latest jettison, where in this context entry is defined as the point at which sensed deceleration first exceeds one Earth g. Nominal event times of E+140 s and E+150 s were then selected, and the resulting trajectory is shown in Fig. 2. Similar analysis was performed for the other EFPAs, with results summarized in Table 3.

Table 2: Summary of SHIELD EDL requirements

Parameter	Requirement
Mach number at drag skirt deployment	≤ 0.9
Time between drag skirt deployment and heatshield jettison	≥ 4 s
Impact velocity	≤ 50 m/s

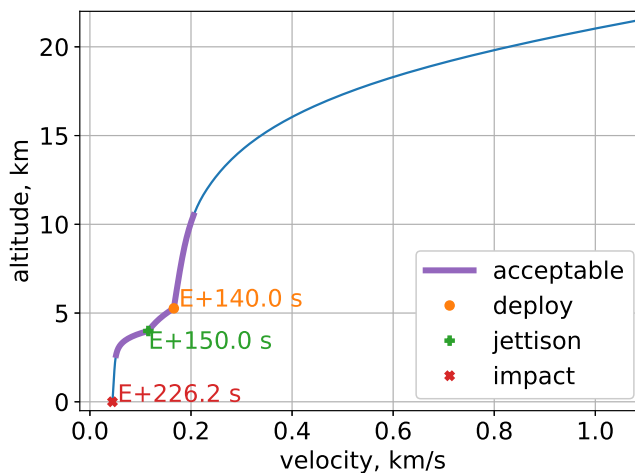


Figure 2: Nominal trajectory, with event timing annotated, for a SHIELD entry at -18° .

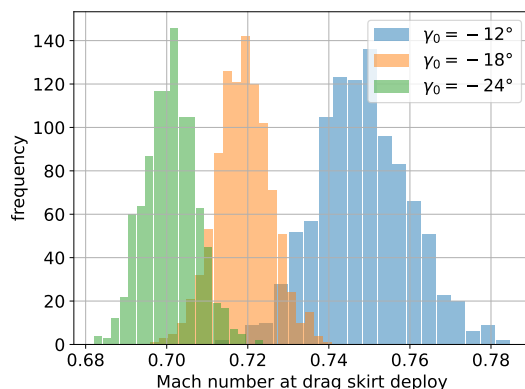
EDL events are often triggered by processed sensor data, such as commanding parachute deployment using either a velocity trigger or range trigger.²⁵ For SHIELD, however, the goal of eliminating

Table 3: EDL event timing, in terms of seconds after entry

EFPA	Earliest Deployment	Latest Jettison	Nominal Deployment	Nominal Jettison
-12°	193.9	258.2	225	235
-18°	105.7	170.9	140	150
-24°	76.9	132.8	105	115

subsystems wherever possible motivates the following question: would a simple timer be sufficient to trigger drag skirt deployment and heatshield jettison without violating the assumed requirements when relevant uncertainties are applied? If so, this could simplify EDL for SHIELD even further.

A 1000-trial Monte Carlo analysis is performed at each of the EFPA values of interest to capture the impact of relevant uncertainties on SHIELD flight-mechanics. In each trial, deployment and jettison are triggered once the nominal time after entry is reached, but the conditions at those points along the trajectory vary due to the input dispersions. Figure 3 shows the resulting Mach numbers at deployment; as can be seen from the histogram, none of the cases for any of the EFPA values exceeded the 0.9 maximum. The requirement on impact velocity was also met, with the maximum value for any of the 3000 total trials being 45.9 m/s; in fact, impact velocity varied so little that the histograms become unhelpful visualizations and are thus not shown. This is because the probes always proceeded through the EDL stages in time to reach terminal velocity, which only varied slightly. Since the time between deployment and jettison was enforced by the timer itself, we can conclude that for the assumed uncertainties a simple timer is sufficient to trigger EDL events while meeting requirements. This result is largely because the acceptable timing range is relatively wide.

**Figure 3:** Monte Carlo results for Mach number at drag skirt deployment at varying EFPA.

Another relevant constraint, peak heat flux, is reported in Fig. 4a. As expected, steeper EFPA values result in higher heating as deceleration occurs more rapidly. No requirement on peak heat flux is assumed for SHIELD in this study, but these values are reported for reference. Additionally, histograms of landing error are shown in Fig. 4b, where error is defined as the distance between the nominal and actual landing sites. Note that there is a major decrease in landing error as the EFPA gets steeper from -12° to -18° , and that while there is a further decrease for an EFPA of -24° the returns are diminishing after some point. Table 4 summarizes the results of these Monte Carlo analyses.

Finally, note that this study also examined the possibility of using drag skirt deployment and

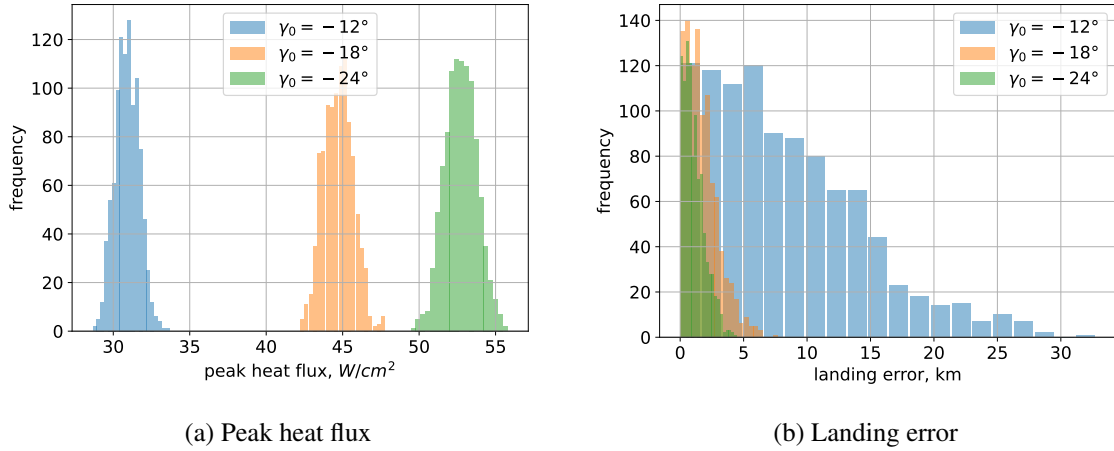


Figure 4: Monte Carlo results at varying EFPAs

Table 4: Summary of Monte Carlo results for EDL of a single SHIELD probe

EFGPA	Mach at Deployment		Impact Velocity, m/s		Peak Heat Flux, W/cm ²		Landing Error, km	
	Mean	STD	Mean	STD	Mean	STD	Mean	STD
-12°	0.748	0.0115	44.6	0.801	30.9	0.777	8.29	6.06
-18°	0.719	0.00672	44.7	0.792	44.7	0.962	1.70	1.27
-24°	0.701	0.00636	44.6	0.783	52.7	1.04	1.12	0.829

heatshield jettison as a method of control. By carefully timing these events based on the difference between the nominal and estimated states for the current time, the vehicle could in theory adjust its landing site in the +/- along-track direction. In practice, however, the requirement that the drag skirt deploy in subsonic conditions severely limits the total achievable control authority, to the extent that this approach has no merit for this application. This is because by the time the vehicle reaches subsonic speeds it has already dissipated almost all of its energy and is at a low altitude (about 10 km in this case), leaving little time or energy for the change in ballistic coefficient to significantly impact the landing site. Specifically, for two trajectories at an EFGPA of -18° , one with the earliest permissible deployment and jettison times and the other with the latest permissible times, the two trajectories land only about 3 km apart. This represents the maximum possible control authority yielded by this method, and because this is well below the expected landing site dispersions the approach is discarded as a method of flight-control. If the drag skirt could be deployed at supersonic or hypersonic speeds the control authority would increase substantially and this method would merit reexamination, but the current drag skirt concept would not structurally or thermally withstand such conditions.

REGIONAL PROBE NETWORKS

This section investigates maneuver design and performs uncertainty quantification for regional networks, and primarily consists of results originally presented in Ref. 26. Regional networks are loosely defined as having all probes within 100 km of the central landing site. Because the changes in trajectory to achieve these separations are relatively small, the relationship between separation time and separation distance, as well as that between jettison speed and separation distance, is

roughly linear. A linearized numerical targeting method is therefore developed and employed to design maneuvers for a reference network, then these trajectories are subjected to relevant uncertainties to quantify the impact of these dispersions on probe landing locations.

The linearized targeting method for regional networks is summarized as follows. Take $\mathbf{x}_{\theta\phi} = [\theta, \phi]^T$ to be landing site coordinates and $\mathbf{V} = \mathbf{V}(t)$ to be the velocity of the probe at some time prior to landing. Apply a Taylor series expansion to $\mathbf{x}_{\theta\phi}$ about the trajectory of the carrier spacecraft, $\mathbf{x}_{\theta\phi}^*$, as a function of velocity, then neglect terms of second order or higher:

$$\mathbf{x}_{\theta\phi} = \mathbf{x}_{\theta\phi}^* + \left. \frac{\partial \mathbf{x}_{\theta\phi}}{\partial \mathbf{V}} \right|_* (\mathbf{V} - \mathbf{V}^*) + \text{H.O.T.s} \quad (2)$$

$$\Delta \mathbf{x}_{\theta\phi} \approx \left. \frac{\partial \mathbf{x}_{\theta\phi}}{\partial \mathbf{V}} \right|_* \mathbf{V}_j = [\mathbf{J}] \mathbf{V}_j \quad (3)$$

$$[\mathbf{J}] = \begin{bmatrix} \frac{\partial \theta}{\partial V_x} & \frac{\partial \theta}{\partial V_y} & \frac{\partial \theta}{\partial V_z} \\ \frac{\partial \phi}{\partial V_x} & \frac{\partial \phi}{\partial V_y} & \frac{\partial \phi}{\partial V_z} \end{bmatrix}_* \quad (4)$$

where the jettison velocity is the velocity of the probe minus the velocity of the carrier spacecraft at the moment after jettison, $\mathbf{V}_j = \mathbf{V} - \mathbf{V}^*$. The Jacobian matrix $[\mathbf{J}]$ can then be evaluated for any value of jettison time to represent the sensitivity of landing site coordinates to velocity at that time. By inverting the Jacobian, the \mathbf{V}_j vector required to achieve a desired change in landing location, $\Delta \mathbf{x}_{\theta\phi}$, can be linearly approximated. The Jacobian in this case is not square, so the least-norm solution is selected to minimize \mathbf{V}_j magnitude.

$$\mathbf{V}_j = [\mathbf{J}]^T ([\mathbf{J}][\mathbf{J}]^T)^{-1} \Delta \mathbf{x}_{\theta\phi} \quad (5)$$

For the purpose of this study, $[\mathbf{J}]$ is numerically approximated using first-order forward finite differencing; Eq. 6 gives an example for the first element of the matrix,

$$\frac{\partial \theta}{\partial V_x} = \frac{\theta_p - \theta^*}{\Delta V_x}, \quad (6)$$

where ΔV_x is a small velocity perturbation in the x-axis direction and θ_p is the landing site longitude that results from applying a jettison velocity of $[\Delta V_x, 0, 0]^T$ then propagating to surface impact. In this study, a perturbation value of $\Delta V_x = \Delta V_y = \Delta V_z = 1 \times 10^{-4} \text{ m s}^{-1}$ was selected. Numerically computing the Jacobian $[\mathbf{J}]$ according to Eqs. 4 and 6 allows one to linearly approximate the jettison velocity vector \mathbf{V}_j required to achieve a shift in longitude and latitude equal to $\Delta \mathbf{x}_{\theta\phi} = [\Delta \theta, \Delta \phi]^T$ for a given separation time. To consider a different jettison time, the Jacobian is simply re-evaluated applying perturbations at that time.

This linearized targeting method is employed to design maneuvers for a regional network. As a motivating example, the reference science mission is a seismology network deployed to Cerberus Fossae, a region of known seismicity on Mars.^{27,28} A regional network in such an area can obtain useful geophysical measurements using significantly lower sensitivity seismometers than a global network would require by relying on its proximity to seismic events, bringing the required payload mass down to the range of 2–3 kg per lander*.²⁹ Shock-tolerant seismology payloads have been developed that can survive 15,000 g's at impact,³⁰ and precision landing of probes is significantly less important than achieving a network geometry that permits observability.

*This assumption on total payload mass for a seismometer of the required sensitivity is based on the short-period instrument aboard the InSight lander and private communications with Mark Panning, Dec. 2021.

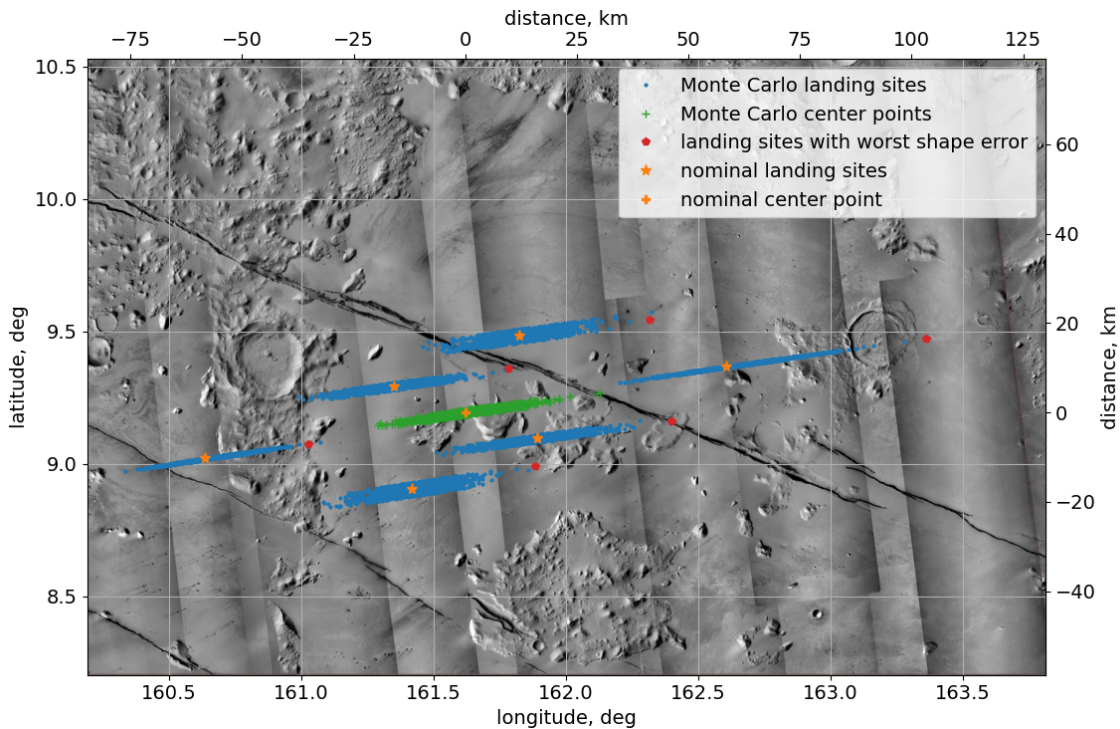


Figure 5: Nominal and random trial landing locations shown against to-scale Martian surface.

To target Cerberus Fossae, the central entry state is defined to have an entry longitude of 150° East, entry latitude of 7.25° North, EFPA of $\gamma_0 = -12^\circ$, and entry heading angle of 80° (slightly Northward of due-East). The network consists of three pairs of probes such that each pair is targeted with equal and opposite jettison velocities $\pm \mathbf{V}_j$, resulting in a symmetrical network of six probes. The separation timing is varied such that all jettison velocities have a magnitude of 10 cm/s , resulting in separation times ranging from 3.136 to 0.821 days before entry; see Ref. 26 for further detail.

The results of applying relevant uncertainties to this reference scenario in a 1000-trial Monte Carlo analysis are shown in Fig. 5*. As expected based on intuition and the earlier flight mechanics analysis, the probes experience large dispersions in landing site, primarily in the along-track direction. However, it turns out that these dispersions are highly-correlated between probes for any given trial, because all dispersions except jettison speed and ballistic coefficient apply to the trial as a whole and affect all of the probes in more or less the same way. For this scenario, dispersions on jettison speed have relatively little effect because the nominal speeds are low enough to be within the regime of roughly linear sensitivity for these trajectories. As a result of all this, the network shifts back-and-forth in along-track but its shape deforms relatively little. This effect is captured by defining a shape error parameter to quantify this deformation, and the landing locations for the trial with the largest shape error are shown in the red pentagons in Fig. 5. It can be seen by inspection that the network shape in this trial is qualitatively similar to the nominal shape, but with an offset in the positive along-track direction. See Ref. 26 for more detail on center vs. shape error. The key

*These results are nearly identical to Fig. 8 in Ref. 26, except they correct a simulation error that prevented density from being correctly dispersed in the previous work.

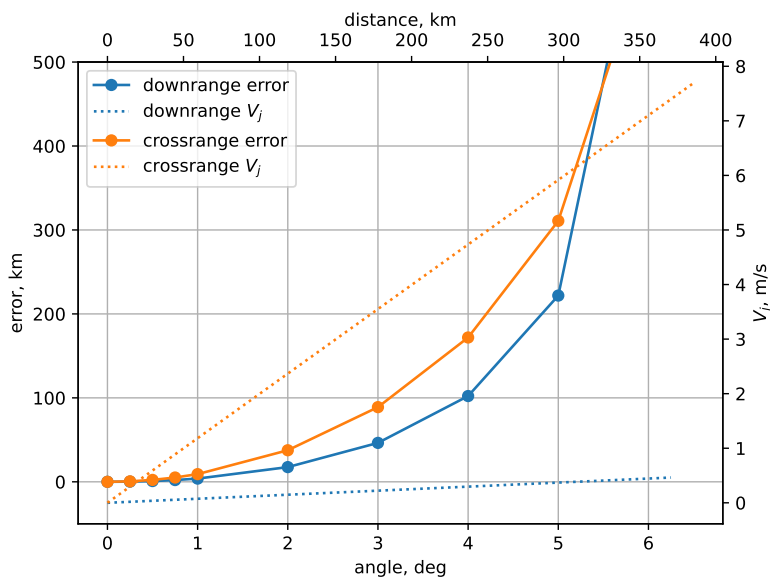


Figure 6: Error and required V_j for linearized targeting for varying downrange and crossrange spacing. After the desired change in angle exceeds 6.5° , both cases begin to miss the planet entirely.

takeaway is that, for the example regional network considered here, the probes can be delivered to roughly the desired arrangement on the surface despite large dispersions for each individual probe, so long as roughly ± 25 km along-track shifts of the entire network can be tolerated.

The linear approach to targeting applied in this section is a good approximation only within some local region of the reference trajectory, that is, near the approach trajectory of the carrier spacecraft leading to the center entry point. Thus, it is important to quantify the limits of applicability for the linearization, and the results of this analysis are shown in Fig. 6. Note that these results are generated for the approach trajectory used in the reference regional network scenario described above for a separation time of one day before entry. From these results, it is clear that after about 100 km of desired separation distance the linearization begins to degrade rapidly. By about 300 km of desired separation the targeting error is of similar magnitude to the desired separation, and beyond this point the probes begin missing the planet entirely when the jettison velocity computed by the linearized targeting method is employed.

LARGE-SCALE PROBE NETWORKS

The linearization method presented in the previous section fails for networks that extend beyond about 100 km from the central point, requiring a different approach. In this section a numerical nonlinear optimization tool* is applied to design maneuvers for large-scale networks of co-delivered probes, then a similar uncertainty quantification analysis is performed. For these scenarios a more generic entry state of 0° longitude, 0° latitude, and 90° (due-East) heading angle is assumed, such that along-track and cross-track are directed East-West and North-South, respectively. Along-track and cross-track separations are treated separately in this analysis based on the significant difference in required jettison speed, as shown in Fig. 6; this is also intuitive from orbital mechanics, which

*specifically, `scipy.optimize.minimize`

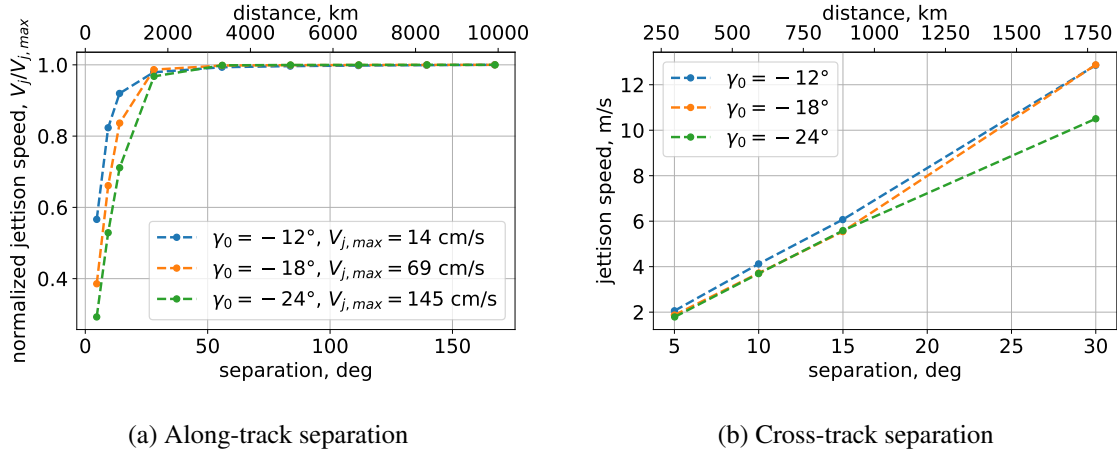


Figure 7: Required jettison speed vs. desired landing separation, for separation 3 days before entry and varying EFPAs

instruct that changing the plane of motion in general takes greater effort than changes of similar magnitude within the plane of motion.

Figure 7 explores the relationships between desired separation, required jettison speed, and EFPA for both along- and cross-track separations, with separation performed three days before entry. As expected, larger separations tends to require larger jettison speeds. This relationship takes a roughly linear form for cross-track separations, shown in Fig. 7b, despite the breakdown of the linearization method based on finite-differencing from small perturbations. Furthermore, the EFPA of the approach trajectory has very little effect on the required jettison speed. In sharp contrast, the jettison speed required for along-track separations asymptotically approaches a fixed value beyond about 25 degrees of separation, and is strongly affected by approach trajectory EFPA. Note that the y-axis of Fig. 7a is normalized with respect to the required jettison time of the largest separation, highlighting the similarity in shape between the different EFPAs despite their offset values, whereas Fig. 7b shows non-normalized speeds.

Insight into the unusual trends for along-track separation can be gained from examining the trajectories themselves. Figure 8a shows planet-relative motion in the altitude vs. downrange plane, and Fig. 8b shows trajectories in the planet-centered inertial frame. The three cases with smallest separations can be seen to follow similarly-shaped trajectories down to the surface, separated due to offsets in their exoatmospheric trajectories and incremental changes in their entry states. The rest of the trajectories, however, enter the atmosphere on nearly the same trajectory and then achieve separation during atmospheric flight, with each subsequent trajectory coasting for longer in the atmosphere. Eventually, for the greatest along-track separations, the probes follow skip-out trajectories that leave the atmosphere then re-enter.

Thus, there is a characteristic difference between the along-track separations for up to about 15 degrees and those for separations of 30 degrees or more. In the former case, along-track extension is achieved via incremental offsets in entry state, including entry flight-path angle, due to changes in the exoatmospheric trajectory. For the larger separations, tiny differences in entry state yield dramatically different atmospheric trajectories, such that each successive coast phase is longer. Harnessing

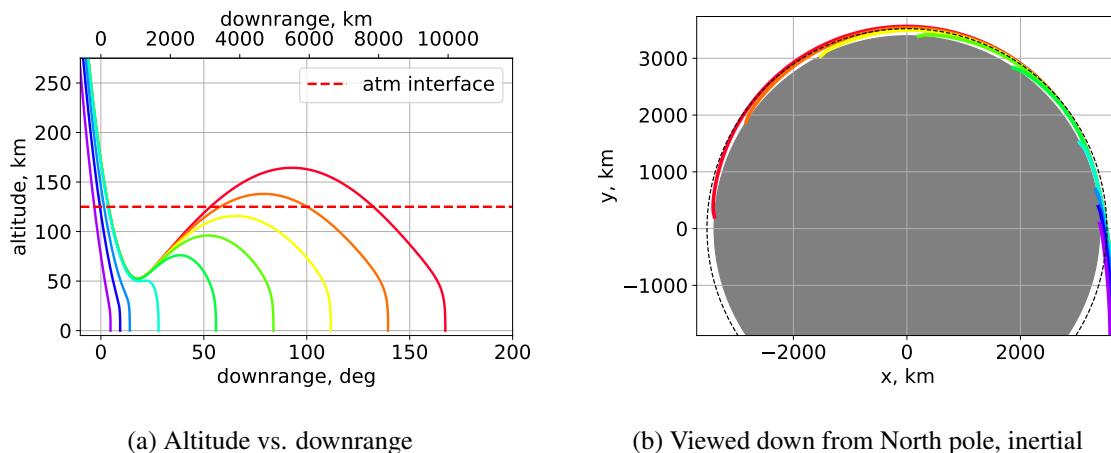
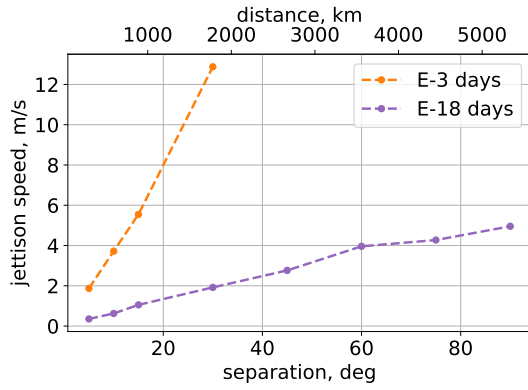


Figure 8: Probe trajectories for along-track separations ranging from 5° (purple) to about 165° (red)

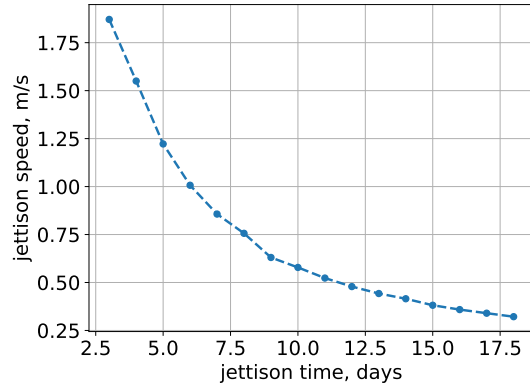
the atmospheric flight mechanics in this way enables large separations with relatively small jettison speeds, and also explains why the EFPA of the approach trajectory significantly impacts required jettison speed. Because the dynamics become so sensitive to the entry state, the respective jettison velocities required for 30 degrees or 60 degrees of along-track separation are almost identical, just with a slightly greater magnitude for the 60 degree case. In contrast, cross-track separation is achieved primarily by modifying the exoatmospheric trajectory, and is thus insensitive to approach trajectory EFPA.

All of the large-scale network results thus far assume a separation time of three days before entry, so it is instructive to consider the relationship between separation time and required jettison speed, particularly for cross-track separation since the required speeds are larger in this case. To this end, Fig. 9a compares the required jettison speed vs. desired separation for separation events 3 and 18 days before entry. The required speeds for 18 days before entry are not only lower, but also increase at a slower rate compared to separation 3 days beforehand. Figure 9b shows how required jettison speed changes with varying separation timing for a 5° cross-track separation; one can imagine this as representing the continuum between the leftmost points of the two lines in Fig. 9a. As shown for regional networks in Ref. 26, the required jettison speed decreases monotonically and nonlinearly as the time between separation and entry increases.

The preceding results demonstrate the ability to use nonlinear numerical optimization to design maneuvers to co-deliver large-scale probe networks. To understand the practicality of these trajectories, however, the impact of relevant uncertainties must be considered. A 1000-trial Monte Carlo analysis is performed for this purpose, assuming an EFPA of -18° and using the same input dispersions as in the previous section. In this case eight total probes are considered; four probes with increasing along-track separations of approximately 5, 9, 14, and 26 degrees, and four probes with increasing cross-track separations of approximately 5, 10, 15, and 30 degrees. The along-track separations occur 3 days before entry, and the cross-track separations occur 18 days before entry. Figure 10 shows the resulting landing error for these 8 probes, and Fig. 11 shows the resulting EFPAs. It should be reiterated that EFPA of the central approach trajectory, which is the same for all cases, is distinct from the actual flight-path angle of each probe upon entering the atmosphere.

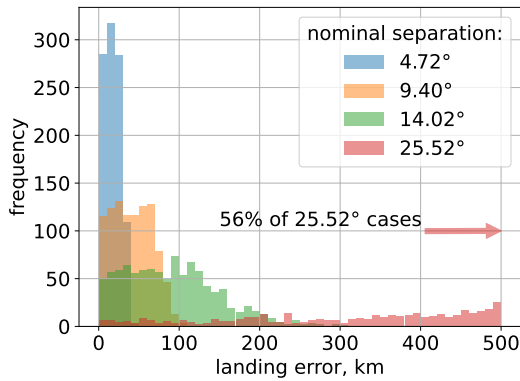


(a) Varying cross-track separation

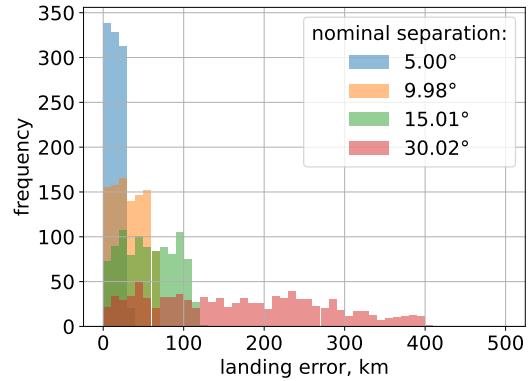


(b) 5° cross-track separation

Figure 9: Comparisons of required jettison speed at varying separation times, for an EFPA of -18°



(a) Along-track separations



(b) Cross-track separations

Figure 10: Monte Carlo results for large-scale network. For the largest along-track separations, about 29% of total cases (roughly half of those not shown) miss the planet entirely.

From Fig. 10a, it is clear that landing error increases substantially with each increase in nominal separation. The landing dispersions for the 9 and 14 degree cases are large but bounded, such that they would conceivably still suffice if the probes were targeting a broad region on the surface. In contrast, the 26 degree case has such large landing error that 29% of cases miss the planet entirely, and almost 60% of all cases have greater than 500 km error. This large jump in error statistics is the result of the plateau in required jettison speed observed in Fig. 7a. Because very small changes in jettison speed result in huge changes in landing separation, the $\pm 10\%$ maneuver dispersion is sufficient to radically degrade targeting. Clearly, under the assumed scenario and dispersions, the 26° along-track separation is not a viable trajectory, nor are the trajectories with greater along-track separation.

To get a sense of to what extent the error results from jettison speed dispersions, Fig. 12 shows the results of an equivalent Monte Carlo analysis but without maneuver dispersions. All probe

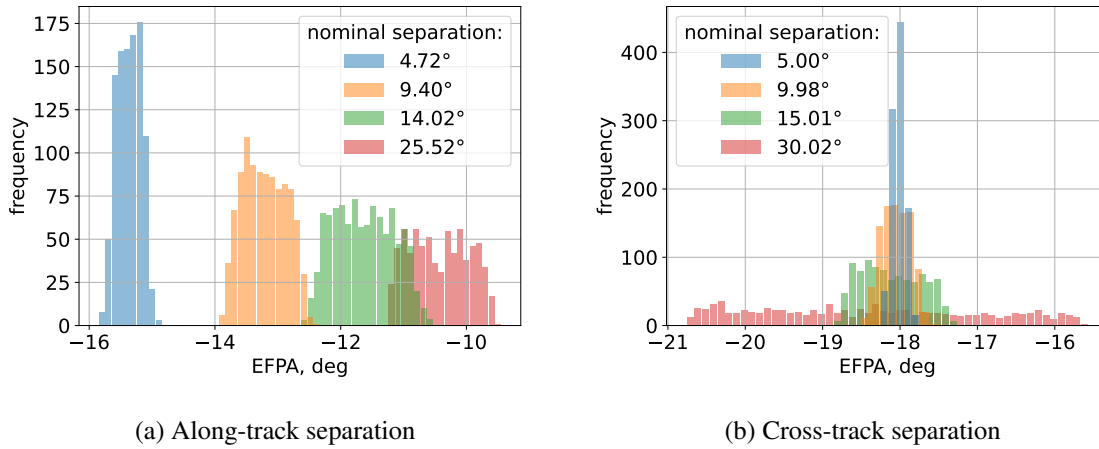


Figure 11: Actual entry flight-path angles (EFPAs) for probe trajectories

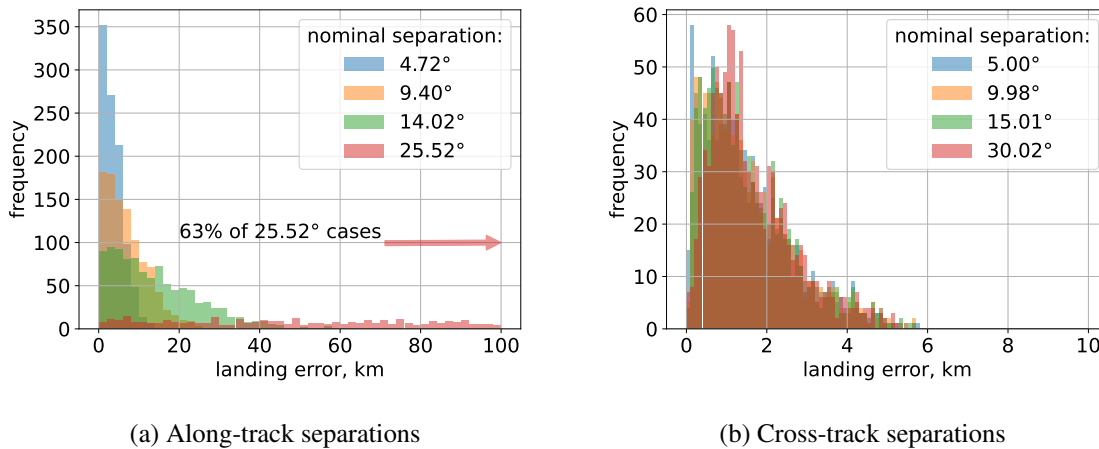


Figure 12: Monte Carlo results for large-scale network without maneuver dispersions

trajectories show marked improvement, including the 26 degree case, and no trajectories miss the planet. However, the 26° case still has dramatically greater landing error than the other three cases. This is because the trajectory’s extended coast phase, as seen in Fig. 8, results in a trajectory that is fundamentally more sensitive to variations. That is, even when perfect maneuver execution is assumed, small variations have a major impact due to the shallow EFPA and close proximity to other trajectories in the solution family that extend much further in along-track.

Turning to the cross-track, the landing error with dispersed jettison speed also increases substantially as desired separation increases, with the 30° case again performing much worse than the other three probes but this time without any errors exceeding 500 km. However, in contrast to the along-track cases, the landing error results for the Monte Carlo analysis without maneuver dispersions are relatively small and seemingly insensitive to desired separation. The differing behavior comes down to nominal EFPA for each probe. As shown in Fig. 11a, as desired along-track separation

increases the nominal EFPA becomes shallower and EFPA dispersions become larger*. Figure 11b shows that the cross-track trajectories, in contrast, all have a mean EFPA of about -18° , the same as the central approach trajectory, but the dispersions still increase with desired separation. The dispersions increase as the nominal jettison speed increases with desired separation and thus the maneuver dispersions have greater effect, but because of the difference in how cross-track separations are targeted the nominal EFPA is mostly unchanged. Thus, when maneuver execution error is removed from the assumed dispersions, all cross-track trajectories enter at about -18° and experience landing error consistent with the single-probe flight mechanics analysis shown in Fig. 4b. The larger EFPA dispersions resulting from maneuver execution error for the 30° cross-track case are what account for the much greater landing site dispersions seen in Fig. 10b; although this case is benign compared to the largest along-track separation case, it still is most likely too much error for practical application.

CONCLUSIONS

Networks of co-delivered probes on the Martian surface would be scientifically valuable at a range of scales, and this study examines some of the relevant flight mechanics and mission design considerations. It is shown that regional networks within about 100 km of the central point can be co-delivered with a small mechanical jettison within five days of atmospheric entry. Larger networks ranging up to global in size are considered and trajectories are successfully identified using numerical nonlinear optimization. However, under the study's assumptions, including separation no earlier than 20 days before entry and a $\pm 10\%$ uniform dispersion on jettison speed, probe trajectories beyond a certain separation distance are too sensitive to error to be practical. For the scenario considered here, for along-track separations this cutoff occurs roughly between 15 and 20 degrees of desired separation, and for cross-track separations the equivalent threshold is somewhere between 15 and 30 degrees. Several alternative approaches could potentially enable larger separations. The strict co-delivery assumption could be relaxed to allow the carrier spacecraft to perform multiple maneuvers during approach, including between separation events. Also, the maneuvers could be performed much earlier, enabling different targeting geometries with much lower required jettison speed compared to similar geometries for separation within 20 days of entry. The targeting optimization process itself could be constrained to solutions with a desired EFPA, resulting in larger separation speeds but avoiding highly sensitive trajectories. Finally, though taking advantage of atmospheric flight dynamics enabled large along-track separation for small jettison speeds, this also resulted in trajectories far too sensitive to small errors; an alternative approach may deliberately not incorporate these dynamics into the targeting scheme.

ACKNOWLEDGMENT

This work was supported by a NASA Space Technology Research Fellowship. S. W. Albert gratefully acknowledges discussion with, and input and aerodynamic data provided by, the SHIELD team at JPL including Louis Giersch, Nathan Barba, Ryan Woolley, and Chad Edwards. S. W. Albert also acknowledges ideas and advice from other participants in the Revolutionizing Access to the Martian Surface workshop organized by the W. M. Keck Institute for Space Studies, as well as at the Low-Cost Science Mission Concepts for Mars Exploration workshop.

*Note, though, that this trend plateaus as separations greater than 26° are targeted, because the differences in entry states for these trajectories are very small.

APPENDIX: EQUATIONS OF MOTION

Take the position coordinates to be radial distance r , longitude θ , and geocentric latitude ϕ . Take the planet-relative velocity coordinates to be velocity magnitude V , flight-path angle γ , and heading angle ψ . The equations of motion for a vehicle in atmospheric flight around an ellipsoidal rotating planet are given below:

$$\dot{r} = V \sin \gamma \quad (7a)$$

$$\dot{\theta} = \frac{V \cos \gamma \sin \psi}{r \cos \phi} \quad (7b)$$

$$\dot{\phi} = \frac{V \cos \gamma \cos \psi}{r} \quad (7c)$$

$$\begin{aligned} \dot{V} = & -D - g_r \sin \gamma - g_\phi \cos \gamma \cos \psi \\ & + \omega_p^2 r \cos \phi (\cos \phi \sin \gamma - \sin \phi \cos \gamma \cos \psi) \end{aligned} \quad (8a)$$

$$\begin{aligned} \dot{\gamma} = & \frac{1}{V} \left[L \cos \sigma + \cos \gamma \left(\frac{V^2}{r} - g_r \right) + g_\phi \sin \gamma \cos \psi + 2\omega_p V \cos \phi \sin \psi \right. \\ & \left. + \omega_p^2 r \cos \phi (\cos \phi \cos \gamma + \sin \phi \sin \gamma \cos \psi) \right] \end{aligned} \quad (8b)$$

$$\begin{aligned} \dot{\psi} = & \frac{1}{V} \left[\frac{L \sin \sigma}{\cos \gamma} + \frac{V^2}{r} \tan \phi \cos \gamma \sin \psi + g_\phi \frac{\sin \psi}{\cos \gamma} \right. \\ & \left. - 2\omega_p V (\cos \phi \tan \gamma \cos \psi - \sin \phi) + \frac{\omega_p^2 r}{\cos \gamma} \cos \phi \sin \phi \sin \psi \right] \end{aligned} \quad (8c)$$

where

$$L = \frac{\rho V^2}{2\beta} L/D \quad (9a)$$

$$D = \frac{\rho V^2}{2\beta} \quad (9b)$$

$$g_r = \frac{\mu}{r^2} \left[1 + \frac{3J_2 R^2}{2r^2} (1 - 3 \sin^2 \phi) \right] \quad (9c)$$

$$g_\phi = \frac{\mu}{r^2} \left[\frac{3J_2 R^2}{2r^2} 2 \sin \phi \cos \phi \right] \quad (9d)$$

REFERENCES

- [1] R. D. Braun and R. M. Manning, "Mars Exploration Entry, Descent, and Landing Challenges," *Journal of Spacecraft and Rockets*, Vol. 44, No. 2, 2007, pp. 310–323, 10.2514/1.25116.
- [2] J. Callahan and C. Dreier, "Mars In Retrograde: A Pathway to Restoring NASA's Robotic Mars Exploration Program," tech. rep., The Planetary Society, 2017.
- [3] A. Elfving, A. L. Elias, M. T. King, G. Lee, J. Pellicciotti, P. C. Theisinger, D. W. Thompson, M. Wadhwa, T. Young, and M. Zuber, "Mars Sample Return (MSR) Program: Final Report of the Independent Review Board (IRB)," tech. rep., NASA, 2020.

- [4] C. J. Culbert, B. L. Ehlmann, and A. A. Fraemen, “Revolutionizing Access to the Martian Surface,” final workshop report, W. M. Keck Institute for Space Studies, 2022, 10.7907/d1sm-mj77.
- [5] D. Banfield, “Mars Science Goals, Objectives, Investigations, and Priorities: 2020 Version,” tech. rep., Mars Exploration Program Analysis Group, 2020.
- [6] S. Diniega, N. Barba, L. Giersch, B. Jackson, A. Soto, S. Rafkin, C. Swann, R. Sullivan, D. Banfield, and L. Fenton, “Optimally-sized Mission Concepts for Focused In-situ Studies of Planetary Surface-atmosphere Interactions,” Oral Presentation, Low-Cost Science Mission Concepts for Mars Workshop, 2022.
- [7] S. C. Stähler, M. P. Panning, D. Antonangeli, W. B. Banerdt, D. Banfield, M. Banks, S. Ceylan, C. Charalambous, J. Clinton, I. Daubar, B. Fernando, D. Giardini, M. Grott, A. Horleston, K. Hurst, T. Kawamura, D. Kim, M. Knapmeyer, R. Lorenz, L. Margerin, A. Marusiak, S. Menina, A. Mittelholz, N. Murdoch, C. Perrin, W. T. Pike, C. Schmelzbach, N. Schmerr, M. Schimmel, A. Spiga, A. Stott, J. Taylor, and R. Weber, “A Cerberus Fossae Seismic Network,” Oral Presentation, Low-Cost Science Mission Concepts for Mars Workshop, 2022.
- [8] S. Rafkin, “The Atmospheric Characterization for Exploration and Science (ACES) instrument suite for Mars,” *2015 IEEE Aerospace Conference*, 2015, pp. 1–6, 10.1109/AERO.2015.7119061.
- [9] C. Nunn, W. T. Pike, I. M. Standley, S. B. Calcutt, S. Kedar, and M. P. Panning, “Standing on Apollo’s Shoulders: a Microseismometer for the Moon,” *The Planetary Science Journal*, Vol. 2, No. 1, 2021, p. 36.
- [10] G. E. N. Scoon and G. P. Whitcomb, “MARSNET: A precursor to the surface exploration of Mars,” *Acta Astronautica*, Vol. 29, No. 10, 1993, pp. 823–831. World Space Congress, 10.1016/0094-5765(93)90164-R.
- [11] S. Squyres, “The Mars environmental survey (mesur) mission,” *Advances in Space Research*, Vol. 15, No. 4, 1995, pp. 179–188, 10.1016/0273-1177(94)00079-G.
- [12] A.-M. Harri, V. Linkin, J. Polkko, M. Marov, J.-P. Pommereau, A. Lipatov, T. Siili, K. Manuilov, V. Lebedev, A. Lehto, R. Pellinen, R. Pirjola, T. Carpentier, C. Malique, V. Makarov, L. Khloustova, L. Esposito, J. Maki, G. Lawrence, and V. Lystsev, “Meteorological Observations on Martian Surface: Met-Packages of Mars-96 Small Stations and Penetrators,” *Planetary and Space Science*, Vol. 46, No. 6, 1998, pp. 779–793, 10.1016/S0032-0633(98)00012-9.
- [13] B. Banderdt, A. F. Chicarro, M. Coradini, C. Federico, R. Greeley, M. Hechler, J. M. Knudsen, C. Leovy, P. Lognonne, L. Lowry, D. McCleese, C. McKay, R. Pellinen, R. Phillips, G. E. N. Scoon, T. Spohn, S. Squyres, F. Taylor, and H. Wanke, “INTERMARSNET: Phase-A Study Report,” Tech. Rep. ESA Publication D/SCI(96)2, European Space Agency, April 1996.
- [14] S. Smrekar, D. Catling, R. Lorenz, J. Magalhães, J. Moersch, P. Morgan, B. Murray, M. Presley, A. Yen, A. Zent, and D. Blaney, “Deep Space 2: The Mars Microprobe Mission,” *Journal of Geophysical Research: Planets*, Vol. 104, No. E11, 1999, pp. 27013–27030, 10.1029/1999JE001073.
- [15] A.-M. Harri, O. Marsal, P. Lognonne, G. Leppelmeier, T. Spohn, K.-H. Glassmeier, F. Angrilli, W. Banerdt, J. Barriot, J.-L. Bertaux, J. Berthelier, S. Calcutt, J. Cerisier, D. Crisp, V. Dehant, D. Giardini, R. Jaumann, Y. Langevin, M. Menvielle, G. Musmann, J. Pommereau, S. Di Pippo, D. Guerrier, K. Kumpulainen, S. Larsen, A. Mocquet, J. Polkko, J. Runavot, W. Schumacher, T. Siili, J. Simola, and J. Tillman, “Network science landers for Mars,” *Advances in Space Research*, Vol. 23, No. 11, 1999, pp. 1915–1924, 10.1016/S0273-1177(99)00279-3.
- [16] A. M. Harri, W. Schmidt, V. Linkin, S. Alexashkin, and L. Vazquez, “MetNet Mars Mission – New Lander Generation for Martian in situ Surface Observations,” *European Planetary Science Congress*, 2012.
- [17] N. Barba, T. Komarek, R. Woolley, L. Giersch, V. Stamenković, M. Gallagher, and C. D. Edwards, “Mars Small Spacecraft Studies: Overview,” *2019 IEEE Aerospace Conference*, 2019, pp. 1–10, 10.1109/AERO.2019.8741735.
- [18] R. D. Braun, R. A. Mitcheltree, and F. M. Cheatwood, “Mars Microprobe Entry-to-Impact Analysis,” *Journal of Spacecraft and Rockets*, Vol. 36, No. 3, 1999, pp. 412–420, 10.2514/2.3461.
- [19] C. Edwards and L. Matthies, “New Capabilities for Accessing the Martian Surface,” tech. rep., Jet Propulsion Laboratory, California Institute of Technology, 2021.
- [20] H. Justh, “Mars Global Reference Atmospheric Model 2010 Version: Users Guide,” Tech. Rep. NASA/TM—2014–217499, NASA, 2014.
- [21] T. J. Martin-Mur, G. L. Kruizinga, P. D. Burkhart, F. Abilleira, M. C. Wong, and J. A. Kangas, “Mars Science Laboratory Interplanetary Navigation,” *Journal of Spacecraft and Rockets*, Vol. 51, No. 4, 2014, pp. 1014–1028, 10.2514/1.A32631.
- [22] D. A. Vallado, *Fundamentals of Astrodynamics and Applications*, ch. Appendix D, pp. 1041–1042. Microcosm Press, 4th ed., 2013.

- [23] C. G. Justus and R. D. Braun, “Atmospheric Environments for Entry, Descent and Landing (EDL),” *5th International Planetary Probes Workshop and Short Course*, 2007, pp. 1–37. <https://ntrs.nasa.gov/citations/20070032693>.
- [24] M. G. Trainer, M. H. Wong, T. H. McConnochie, H. B. Franz, S. K. Atreya, P. G. Conrad, F. Lefèvre, P. R. Mahaffy, C. A. Malespin, H. L. Manning, J. Martín-Torres, G. M. Martínez, C. P. McKay, R. Navarro-González, A. Vicente-Retortillo, C. R. Webster, and M.-P. Zorzano, “Seasonal Variations in Atmospheric Composition as Measured in Gale Crater, Mars,” *Journal of Geophysical Research: Planets*, Vol. 124, No. 11, 2019, pp. 3000–3024, 10.1029/2019JE006175.
- [25] D. Way, “On the use of a range trigger for the Mars Science Laboratory Entry, Descent, and Landing,” *2011 Aerospace Conference*, 2011, pp. 1–8, 10.1109/AERO.2011.5747242.
- [26] S. W. Albert and H. Schaub, “Co-Delivery of Multiple Small Probes to the Martian Surface,” *AIAA SciTech 2022 Forum*, 10.2514/6.2022-1653.
- [27] D. Giardini, P. Lognonné, W. B. Banerdt, W. T. Pike, U. Christensen, S. Ceylan, J. F. Clinton, M. v. Driel, S. C. Stähler, M. Böse, R. F. Garcia, A. Khan, M. Panning, C. Perrin, D. Banfield, E. Beucler, C. Charalambous, F. Euchner, A. Horleston, A. Jacob, T. Kawamura, S. Kedar, G. Mainsant, J.-R. Scholz, S. E. Smrekar, A. Spiga, C. Agard, D. Antonangeli, S. Barkaoui, E. Barrett, P. Combes, V. Conejero, I. Daubar, M. Drilleau, C. Ferrier, T. Gabsi, T. Gudkova, K. Hurst, F. Karakostas, S. King, M. Knapmeyer, B. Knapmeyer-Endrun, R. Llorca-Cejudo, A. Lucas, L. Luno, L. Margerin, J. B. McClean, D. Mimoun, N. Murdoch, F. Nimmo, M. Nonon, C. Pardo, A. Rivoldini, J. A. R. Manfredi, H. Samuel, M. Schimmel, A. E. Stott, E. Stutzmann, N. Teanby, T. Warren, R. C. Weber, M. Wicczorek, and C. Yana, “The seismicity of Mars,” *Nature Geoscience*, Vol. 13, Mar 2020, pp. 205–212, 10.1038/s41561-020-0539-8.
- [28] S. Kedar, M. P. Panning, S. E. Smrekar, S. C. Stähler, S. D. King, M. P. Golombek, M. Manga, B. R. Julian, B. Shiro, C. Perrin, J. A. Power, C. Michaut, S. Ceylan, D. Giardini, P. H. Lognonné, and W. B. Banerdt, “Analyzing Low Frequency Seismic Events at Cerberus Fossae as Long Period Volcanic Quakes,” *Journal of Geophysical Research: Planets*, Vol. 126, No. 4, 2021, p. e2020JE006518, <https://doi.org/10.1029/2020JE006518>.
- [29] P. Lognonné, W. B. Banerdt, D. Giardini, W. T. Pike, U. Christensen, P. Laudet, S. d. Raucourt, P. Zweifel, S. Calcutt, M. Bierwirth, K. J. Hurst, F. Ijpelaan, J. W. Umland, R. Llorca-Cejudo, S. A. Larson, R. F. Garcia, S. Kedar, B. Knapmeyer-Endrun, D. Mimoun, A. Mocquet, M. P. Panning, R. C. Weber, A. Sylvestre-Baron, G. Pont, N. Verdier, L. Kerjean, L. J. Facto, V. Gharakanian, J. E. Feldman, T. L. Hoffman, D. B. Klein, K. Klein, N. P. Onufer, J. Paredes-Garcia, M. P. Petkov, J. R. Willis, S. E. Smrekar, M. Drilleau, T. Gabsi, T. Nebut, O. Robert, S. Tillier, C. Moreau, M. Parise, G. Aveni, S. Ben Charef, Y. Bennour, T. Camus, P. A. Dandonneau, C. Desfoux, B. Lecomte, O. Pot, P. Revuz, D. Mance, J. tenPierick, N. E. Bowles, C. Charalambous, A. K. Delahunty, J. Hurley, R. Irshad, H. Liu, A. G. Mukherjee, I. M. Standley, A. E. Stott, J. Temple, T. Warren, M. Eberhardt, A. Kramer, W. Kühne, E.-P. Miettinen, M. Monecke, C. Aicardi, M. André, J. Baroukh, A. Borrien, A. Bouisset, P. Boutte, K. Brethomé, C. Brysbaert, T. Carlier, M. Deleuze, J. M. Desmarres, D. Dilhan, C. Doucet, D. Faye, N. Faye-Refalo, R. Gonzalez, C. Imbert, C. Larigauderie, E. Locatelli, L. Luno, J.-R. Meyer, F. Mialhe, J. M. Mouret, M. Nonon, Y. Pahn, A. Paillet, P. Pasquier, G. Perez, R. Perez, L. Perrin, B. Pouilloux, A. Rosak, I. Savin de Larclause, J. Sicre, M. Sodki, N. Toulemont, B. Vella, C. Yana, F. Alibay, O. M. Avalos, M. A. Balzer, P. Bhandari, E. Blanco, B. D. Bone, J. C. Bousman, P. Bruneau, F. J. Calef, R. J. Calvet, S. A. D’Agostino, G. d. Santos, R. G. Deen, R. W. Denise, J. Ervin, N. W. Ferraro, H. E. Gengl, F. Grinblat, D. Hernandez, M. Hetzel, M. E. Johnson, L. Khachikyan, J. Y. Lin, S. M. Madzunkov, S. L. Marshall, I. G. Mikellides, E. A. Miller, W. Raff, J. E. Singer, C. M. Sunday, J. F. Villalvazo, M. C. Wallace, D. Banfield, J. A. Rodriguez-Manfredi, C. T. Russell, A. Trebi-Ollennu, J. N. Maki, E. Beucler, M. Böse, C. Bonjour, J. L. Berenguer, S. Ceylan, J. Clinton, V. Conejero, I. Daubar, V. Dehant, P. Delage, F. Euchner, I. Estève, L. Fayon, L. Ferraioli, C. L. Johnson, J. Gagnepain-Beyneix, M. Golombek, A. Khan, T. Kawamura, B. Kenda, P. Labrot, N. Murdoch, C. Pardo, C. Perrin, L. Pou, A. Sauron, D. Savoie, S. Stähler, E. Stutzmann, N. A. Teanby, J. Tromp, M. v. Driel, M. Wicczorek, R. Widmer-Schmidrig, and J. Wookey, “SEIS: Insight’s Seismic Experiment for Internal Structure of Mars,” *Space Science Reviews*, Vol. 215, Jan 2019, p. 12, 10.1007/s11214-018-0574-6.
- [30] T. Hopf, S. Kumar, W. Karl, and W. Pike, “Shock protection of penetrator-based instrumentation via a sublimation approach,” *Advances in Space Research*, Vol. 45, No. 3, 2010, pp. 460–467, 10.1016/j.asr.2009.08.015.